FINAL REPORT : NCC2-5221

Effect of Swirl on Turbulent Structures in Supersonic Jets

by

Ram Mohan Rao

and

Thomas S. Lundgren, P.I.

Department of Aerospace Engineering and Mechanics

University of Minnesota, Minneapolis, MN 55455

March 1998

Abstract

Direct numerical simulation (DNS) is used to study the mechanism of generation and evolution of turbulence structures in a temporally evolving supersonic swirling round jet and also to examine the resulting acoustic radiations. Fourier spectral expansions are used in the streamwise and azimuthal directions and a 1-D b-spline Galerkin representation is used in the radial direction. Spectral-like accuracy is achieved using this numerical scheme. Direct numerical simulations, using the b-spline spectral method, are carried out starting from mean flow initial conditions which are perturbed by the most unstable linear stability eigenfunctions. It is observed that the initial helical instability waves evolve into helical vortices which eventually breakdown into smaller scales of turbulence. 'Rib' structures similar to those seen in incompressible mixing layer flow of Rogers and Moser[1] are observed. The jet core breakdown stage exhibits increased acoustic radiations.

I. Introduction

The object of this work is to obtain highly accurate solutions of turbulent round jets. The solutions obtained help understand the various turbulent scales and mechanisms of turbulence generation in the evolution of a compressible round jet. These accurate flow solutions will be used to estimate acoustic radiation in the near-field region. There has been some work [2-4] in the field of compressible round jets at supersonic Mach numbers but none, to the authors' knowledge, in transition to turbulence in supersonic jets.

Over the past few decades Direct Numerical Simulations (DNS) have become a very powerful tool to obtain highly accurate flow simulations [1,5-9]. In these simulations no models are used, the flow equations are solved using highly accurate numerical schemes. Hybrid spectral methods form a class of such highly accurate numerical methods which have been successfully used by the researchers mentioned above and also by Spalart et al [10]. For the present work a hybrid b-spline spectral method developed by Moser et al [5] is used.

In order to use DNS at high enough Reynolds number to get sufficient turbulent structures the temporal jet problem is studied using periodicity in the axial direction. This allows for the application of spectral expansion in the axial direction. Physically this means that the turbulent structures in the jet are repeated in successive downstream cells and grow in time instead of being gradually modified downstream into a jet plume. There is an approximate correlation between the growth of structures with time in the temporal jet and the growth of structures in the spatially growing jet as one follows the structures downstream. Spectral accuracy helps capture smaller turbulent scales at the expense of some compromise to the overall jet structure.

The compressible round jet is simulated by using Fourier expansions in the azimuthal and streamwise direction and a 1-D b-spline basis representation in the radial direction. The simulation starts with the mean flow, upon which the linear stability eigenfunctions are superimposed, and develops temporally. Various stages of growth, evolution and eventual breakdown of vortical structures are noted. Preliminary acoustic estimates are presented. These give a reasonable picture of the source of most of the turbulent noise and a fair

picture of the directivity of these acoustic waves.

II. Governing Equations

The compressible Navier-Stokes equations written in cylindrical coordinates in non-dimensional form are,

$$\frac{\partial \sigma}{\partial t} = \sigma^2\Big(\frac{1}{r}\frac{\partial (r m_r)}{\partial r} + \frac{1}{r}\frac{\partial m_\theta}{\partial \theta} + \frac{\partial m_z}{\partial z}\Big) \tag{1}$$

$$\begin{aligned}
\frac{\partial m_r}{\partial t} + \frac{\sigma}{r}(m_r^2 - m_\theta^2) &= -\frac{\partial \sigma m_r m_k}{\partial x_k} - \frac{\partial P}{\partial r} + \frac{1}{Re}\Big(\frac{\partial \tau_{rk}}{\partial x_k} + \frac{\tau_{rr} - \tau_{\theta\theta}}{r}\Big) \\
\frac{\partial m_\theta}{\partial t} + \frac{2\sigma}{r} m_r m_\theta &= -\frac{\partial \sigma m_\theta m_k}{\partial x_k} - \frac{1}{r}\frac{\partial P}{\partial \theta} + \frac{1}{Re}\Big(\frac{\partial \tau_{\theta k}}{\partial x_k} + 2\frac{\tau_{\theta r}}{r}\Big) \\
\frac{\partial m_z}{\partial t} + \frac{\sigma}{r} m_r m_z &= -\frac{\partial \sigma m_z m_k}{\partial x_k} - \frac{\partial P}{\partial z} + \frac{1}{Re}\Big(\frac{\partial \tau_{zk}}{\partial x_k} + \frac{\tau_{zr}}{r}\Big)
\end{aligned} \tag{2}$$

$$\frac{\partial P}{\partial t} + \nabla \cdot P\vec{\mathbf{u}} = -(\gamma - 1)P\nabla \cdot \vec{\mathbf{u}} + \frac{1}{Re\ Pr}\nabla \cdot \vec{q} + \frac{(\gamma - 1)}{Re}\Phi \tag{3}$$

where,

$$\frac{\partial}{\partial x_1} = \frac{\partial}{\partial r}\ , \quad \frac{\partial}{\partial x_2} = \frac{1}{r}\frac{\partial}{\partial \theta}\ , \quad \frac{\partial}{\partial x_3} = \frac{\partial}{\partial z},$$

and $\sigma = \frac{1}{\rho}$, $m_k = \rho\ u_k$, $Re = \frac{\rho u r_j}{\mu}$, $Pr = \frac{\mu C_p}{\kappa}$, r_j is the jet radius, Re, Pr are the Reynolds number and Prandtl number, C_p is the specific heat at constant pressure, and Φ is the viscous dissipation given by

$$\begin{aligned}
\Phi =& \mu\Big(2\Big((\frac{\partial u_r}{\partial r})^2 + (\frac{1}{r}\frac{\partial u_\theta}{\partial \theta} + \frac{u_r}{r})^2 + (\frac{\partial u_z}{\partial z})^2\Big) \\
&+ (\frac{1}{r}\frac{\partial u_z}{\partial \theta} + \frac{\partial u_\theta}{\partial z})^2 + (\frac{\partial u_r}{\partial z} + \frac{\partial u_z}{\partial r})^2 + (\frac{1}{r}\frac{\partial u_r}{\partial \theta} + \frac{\partial u_\theta}{\partial r} - \frac{u_\theta}{r})^2 - \frac{2}{3}(\nabla \cdot \vec{\mathbf{u}})^2\Big)
\end{aligned}$$

III. Linear Stability Analysis

Inviscid linear stability analysis is performed for jets with varying degrees of swirl for a Mach 2 jet. In all the cases studied here it is found that the Kelvin-Helmholtz instability

dominates. Helical waves of the form $exp(-k_z z + m\theta)$ where k_z and m are axial and azimuthal wavenumbers, are found to be most unstable with $m \neq 0$. This is similar to the compressible shear layer results of Sandham and Reynolds [8,9], who found that waves oblique to the flow direction were most unstable. The main results of the analysis are shown in fig 1 which shows growth rate versus wavenumber for a series of swirl ratios. It is seen that swirl increases the growth rates of some higher azimuthal disturbances depending on their sense of rotation. From the figure it is also evident that positive swirl while increasing growth rates also shifts the most unstable waves to higher m and k_z, whereas a negative swirl shifts the most unstable modes to lower wavenumbers. This is an interesting result since the addition of positive swirl would encourage shorter waves to grow faster and on the other hand a negative swirl tends to aid the growth of longer waves.

The results obtained from this analysis are used to compute the most unstable eigenfunctions, which are used to perturb the mean flow for non-linear DNS calculations. For details on the stability analysis refer to Rao[11].

IV. Numerical Formulation

The flow variables are expanded using Fourier series in the two periodic directions, *viz.* the azimuthal (θ) and the axial (z) directions. In the non-periodic or radial direction (r) 1-dimensional b-splines are used as interpolating functions.

B-splines [12] of order n are piecewise polynomials of degree n having $n-1$ continuous derivatives. The n^{th} derivative has a jump at knot points within the interval. Since they have a high degree of continuity derivative quantities (like vorticity) can be smoothly and accurately represented. B-splines have local support and hence boundary conditions and any other conditions which are localized can be easily implemented. Also the local support leads to sparse block diagonal matrices which can be efficiently stored and solved.

The continuity equation, for example, can be written in Galerkin form for any k_θ and k_z as

$$\frac{\partial}{\partial t}\,\sigma_i \sum_l \int_R b_i\, b_l\, r dr \;=\; \sum_{j,\,k,\,l} \sigma_i \sigma_j \Big(m_{r_k} \int_R \frac{b_i\, b_j\, (r\, b_k)'\, b_l}{r}\, r dr + \frac{\partial}{\partial \theta} m_{\theta_k} \int_R \frac{b_i\, b_j\, b_k\, b_l}{r}\, r dr \;+\; \frac{\partial}{\partial z} m_{z_k} \int_R b_i\, b_j\, b_k\, b_l\, r dr \Big) \tag{4}$$

where,

$$\sigma \;=\; \sum_k \sigma_k(z,\theta,t)\; b_k(r)\;, \qquad m_\theta \;=\; \sum_k m_{\theta_k}(z,\theta,t)\; b_k(r)\;,$$

$$m_r \;=\; \sum_k m_{r_k}(z,\theta,t)\; b_k(r)\;, \qquad m_z \;=\; \sum_k m_{z_k}(z,\theta,t)\; b_k(r)$$

The Fourier terms are included in the coefficients of the variables, so $\sigma_k(z,\theta,t) = \sigma_k(t) \sum_{k_\theta} \sum_{k_z} exp(ik_\theta\theta + ik_z z)$ and so on.

The derivatives in the θ and z directions are computed by taking a Fast Fourier Transform (FFT) into wave space and multiplying by the appropriate wave numbers (k_θ and k_z), and then an inverse FFT is applied to bring it back to physical space. The momentum and energy equations can be written in a similar manner.

Writing the flow equations as discussed above results in a linear system of coupled equations to solve simultaneously at each time step. Since b-splines of order n have local support on $n+1$ knot (node) intervals this results in a $2n+1$ block banded matrix system,

$$\mathbf{M}\, f \;=\; R, \tag{5}$$

where $\mathbf{M}$ is the resulting mass matrix, f is the column vector of nodal values to be solved for, and R is a column matrix resulting from the RHS of the governing equations. A low storage 3^{rd} order Runge-Kutta scheme designed by Wray [13] is used for time integration.

V. Regularity Requirements and Modal Reduction

In the cylindrical coordinate system the origin ($r = 0$) is a source of concern since some of the functions do not remain analytic. From a mathematical point of view the flow variables should be single valued and finite. To enforce this the polynomial expansion functions must satisfy some regularity requirements [14]. The z-component of the velocity should be represented as,

$$
\begin{aligned}
u_z(r;\ m,k) &= a(m,k)\ r^{|m|}\ P_z(r^2;\ m,k)\ e^{i\ m\theta}\ e^{i\ kz},\ m = all\ \ integers, \\
P_z(0;\ m,k) &= 1,
\end{aligned}
\tag{6}
$$

where $P_z(r^2;\ m,k)$ is a polynomial in r^2. Scalars and z-components of all vectors should be represented in a similar manner. The θ and r-components of the vectors are dependent on each other and should be represented as,

$$
\begin{aligned}
u_r(r;\ m,k) &= b(m,k)\ r^{|m|-1}\ P_r(r^2;\ m,k)\ e^{i\ m\theta}\ e^{i\ kz}, \\
u_\theta(r;\ m,k) &= c(m,k)\ r^{|m|-1}\ P_\theta(r^2;\ m,k)\ e^{i\ m\theta}\ e^{i\ kz}, \\
c(m,k) &= ib(m,k) \quad for\ m\ \geq 1, \\
c(m,k) &= -ib(m,k) \quad for\ m\ \leq -1, \\
P_r(0;\ m,k) &= P_\theta(0;\ m,k) = 1,
\end{aligned}
\tag{7}
$$

for $m = 0$ $b(m,k)$ and $c(m,k)$ are unrelated.

Another problem arising from a cylindrical mesh is that the aspect ratio of the cells near the origin gets very large. The number of azimuthal modes near the origin have to be reduced to maintain a good CFL number. This is referred to as mode suppression. The number of azimuthal modes are effectively reduced to 2 near the origin and are increased successively until the outer boundary has all the azimuthal modes. This reduces the accuracy near the axis but increases the allowable time-step, dt, by a significant amount.

Both of these conditions give rise to a set of constraint equations which are implemented by replacing some rows in the mass matrix and suitably modifying the RHS vector R [7,11].

VI. Boundary conditions

In solving a temporally evolving jet the inflow-outflow boundaries are made periodic (see fig 2). This also enables us to use a spectral expansion in the axial direction and also takes care of the inflow-outflow boundary conditions. The only boundaries of concern are the radial numerical boundaries where a first order non-reflecting boundary condition

for outflow has been used. This condition prevents incoming waves from infinity by using one-dimensional Riemann invariants. This takes the form,

$$\frac{\partial}{\partial t}p' - \rho_\infty c_\infty \frac{\partial}{\partial t}u'_r = -\frac{c_\infty}{2\ R}p' \tag{8}$$

where R is the radius of the outer boundary, and the primed quantities represent perturbations from the ∞ quantities, which represent the free stream quantities. The term on the right hand side is a correction for a cylindrical boundary. Similar conditions are obtained by Engquist and Majda [15,16] and Giles [17]. This boundary condition works well for directly incident waves. For the present case the above conditions serve the purpose since the jet flow has nearly cylindrical wavefronts incident on the boundary. In addition the outgoing wave amplitudes have been mitigated by numerical dissipation due to coarsening of the mesh gradually as the outer boundary is approached.

VII. The DNS of the Swirling Jet

VII a) Initial Conditions and Computational Domain SetUp

The simulation is started with a base flow having a half-Gaussian (see fig 3.) axial velocity profile with a maximum centerline velocity of Mach 2 and a tangential velocity such that there is solid body rotation in the jet core and maximum swirl in the jet shear layer diminishing to zero outside of the jet shear layer. This is achieved simply by setting $\bar{U}_\theta = Sr\bar{U}_z$, where S is a factor used to control the amount of swirl (also called swirl ratio). For this simulation S is set to 0.4. The radial mean flow velocity is set to zero. Uniform mean temperature is assumed across the jet. The mean pressure $\bar{P}$ depends on the radial coordinate r, and hence so does the mean density $\bar{\rho}$. When the mean flow parameters are used to satisfy the Euler equations a relation for $\bar{P}$ is obtained ;

$$\frac{d\bar{P}}{dr} = \frac{\bar{\rho}\bar{U}_\theta^2}{r}. \tag{9}$$

From the equation of state (non-dimensionalized)

$$\bar{\rho} = \frac{\gamma \bar{P}}{\bar{T}}. \tag{10}$$

Using the above equation in equation 10 it can be shown that

$$\bar{P}(r) = P_\infty e^{-\int_r^\infty \frac{\gamma \bar{U}_\theta^2}{r\bar{T}} dr}. \tag{11}$$

where $\bar{T}$ is a constant set to 1, $\bar{U}_\theta$ is a known function of r, and $P_\infty = \frac{1}{\gamma}$ from non-dimensionalization. Once $\bar{P}(r)$ is computed, $\bar{\rho}$ can be computed from equation 11.

The density is non-dimensionalized with ρ_∞, and the temperature by T_∞. Pressure is non-dimensionalized by $\rho_\infty a_\infty^2$, where a_∞ is speed of sound at infinity. The dimensionless mean flow temperature and hence the speed of sound are set to 1. The same mean flow conditions are used for the linear stability analysis in section III. The mean flow quantities $\bar{\sigma}$,$\bar{m}_\theta$, $\bar{m}_z$, $\bar{P}$ are perturbed by the most unstable linear stability eigenfunctions, computed in section III (σ', u'_θ, u'_r, u'_z, and p'), giving initial conditions :

$$\begin{aligned}
\sigma &= \frac{1}{\bar{\rho}} + \sigma' \\
m_\theta &= \bar{m}_\theta + m'_\theta \quad (= \bar{\rho}\bar{U}_\theta + \rho'\bar{U}_\theta + \bar{\rho}u'_\theta) \\
m_r &= m'_r \quad (= \bar{\rho}u'_r) \\
m_z &= \bar{m}_z + m'_z \quad (= \bar{\rho}\bar{U}_z + \rho'\bar{U}_z + \bar{\rho}u'_z) \\
P &= \bar{P} + p'
\end{aligned} \tag{12}$$

The maximum amplitude of these perturbations is taken to be 0.05.

Though the most unstable eigenvalues for a $S = 0.4$ occur for $m = 5$ at $k_z = 5.5$ (fig 2.), $m = 4$ and $k_z = 3$ eigenfunctions are used in order to keep the computation similar to the non-swirling jet case simulated by Rao [11]. The domain size is chosen to accommodate one wavelength of the $m = 4$ and $k_z = 3$ disturbance wave in both the θ and z directions, so a quarter domain is simulated in the θ direction and the computational domain length in the axial direction is $L_z = \frac{2\pi}{k_z}$. This greatly reduces the size of the simulation and allows better resolution for smaller scales. In this case however, the most unstable waves have higher frequencies or lower wavelength in the θ and z directions. Hence due to the

fluid physics, more unstable mode waves with higher frequencies can be generated, and if they grow faster than the $m = 4$ and $k_z = 3$ waves, the domain can exhibit more than one wavelength of these shorter wavelength waves. There is thus a possibility for multiple structures with this shorter wavelength to evolve, and thus the possibility of capturing vortex pairing dynamics if two vortex structures develop in one domain length. This is indeed the case as will be seen below in section VIIb. The outer domain is chosen at 4 jet radii ($R = 4r_j$). This is considered far enough not to encounter any mass flow across the boundary. The non-reflecting boundary conditions are applied at this boundary.

The Reynolds number (Re) for the simulation based on jet radius (r_j) and speed of sound in the core ($\bar{a}$) is kept the same at 2500. The simulation is started from a coarse mesh which is refined as the simulation progresses. The resolution requirements are controlled by monitoring the energy spectra and also by visual inspection of the flow field. It is noted that maximum resolution is needed during transition. The final maximum resolution used is $128 * 167 * 144$ ($N_\theta * N_y * N_z$). 128 Fourier modes represent a quadrant in the azimuthal direction, 167 b-splines in the radial direction from 0 – R, and 144 Fourier modes in the axial direction over L_z are used. The mesh is non-uniform in the radial direction with more clustering in the jet shear layer.

VII b) The DNS Results

The evolution of the swirling jet is shown in figures 4a and 4b as a reconstruction of the temporal jet, constructed by placing temporal sections from different times adjacent to each other. The convective velocity of the large scale structures is used for the reconstruction. The density plot (fig. 4a) clearly outlines the different stages of evolution. The initial frames show a uniformly varying density from the axis to the shear layer, until t = 5.2 which marks the commencement of core breakdown. Also clearly visible is the edge of the jet shear layer. The last two frames show flow without much of a core. Some Mach waves can be seen in the last few frames after core breakdown (seen more clearly in a similar pressure plot shown below in fig 14).

The vorticity magnitude plot (fig. 4b) illustrates an initially sharp shear layer with

helical instability waves developing into helical vortices. There is distinct formation of roller at time t = 2.6. Since the domain size is such that it supports a wavelength of the disturbance smaller than its length (explained above in VIIa) there is the formation of two rollers (also seen in the $r - \theta$ cross-section plot fig. 9a). These rollers eventually pair and this pairing mechanism can be clearly seen at t = 3.9. The pairing is complete by t = 5.2 leaving only one large scale structure, and by t = 6.5 this structure rolls up into a large roller. At t = 7.8 the roller has broken into smaller more intense vortices.

The energy spectrum is plotted versus the axial (fig. 5a) and the azimuthal (fig. 5b) wave numbers at different times. The solid line shown is the $k^{-5/3}$ spectrum. A broad energy spectrum is observed even though the initial conditions had energy only in the k_z = 1 and k_θ = 1 modes. This indicates that the energy has been cascaded to other scales as the jet developed.

Figure 6, shows variation of mean axial velocity with radius over time. This is used to monitor the growth in the mean thickness of the shear layer at different times of the simulation. The shear layer which was initially about $0.2r_j$ reaches $2.0r_j$ at core collapse.

Since only a $m = 4$ mode is used to perturb the mean flow, the ensuing flow will have a quarter domain symmetry in the azimuthal direction. Thus flow is computed only in one quadrant. The other quadrants would have identical flow fields. Hence we plot only one quadrant. The instability waves are tracked from initial time through a sequence of vorticity iso-surface plots with a few cross-sectional plots for emphasis.

At t = 0 (fig 7), the iso-surface plots show a flat vortex sheet with a strong helical wave instability on it. By t = 1.3 (fig 8) the development of multiple helical disturbances is clearly visible. This indicates the start of the evolution of the shorter wavelength disturbances. This is when the faster growing instability waves (higher frequency) begin to dominate the flow. The higher vorticity ($\omega = 12$) is tube-like and sheathed between the lower vorticity ($\omega = 6$) sheets. These waves become more pronounced at t = 2.6 (fig 9b). There is a distinct roll-up of the helical instability waves into helical vortex tubes. Two vortex rollers both in the $r - \theta$ (fig 9a) and $r - z$ cross-sections (see fig 4b) are clearly seen. This allows the phenomenon of vortex-pairing. The vortex sheets in the region between the

two rollers (this has been called the braid region by some researchers) exhibit secondary instabilities. Pairing can be seen between the two helical vortex rollers at t = 3.9 (fig 10a - 10b and 4b). These rollers begin merging into one large scale structure. The vorticity is still concentrated in long vortex-sheet like structures. Intense vortex tubes or 'ribs', which are oriented almost perpendicular(locally) to and wrap around the primary helical vortex, can initiate in the braid region between the two rollers. (Rogers and Moser [6], noted very intense round 'ribs' or streamwise vortices wrapping around large scale spanwise rollers in their incompressible mixing layer flow.) These 'ribs' develop circular cross-sections as they intensify.

By t = 5.2 (fig 11a-11c) the pairing mechanism is complete and the large scale structure has started breaking down into smaller more intense vortical structures. This is a rapid transition region and is characterized by large acoustic radiations, as will be shown in the next section. The $r-\theta$ cross-section shows formation of spiral S-shaped vortex cores along the outer edge of the shear layer. These intense vortex cores roll the flat vortex sheets around them. These are 'rib' cross-section signatures. The 'ribs' are clearly visible in the iso-surface plots ($\omega = 6$) as the two large vortex tubes wrapping around the primary vortex tube in the opposite sense of the helix †. The primary helical vortex is seen more clearly in the $\omega = 12$ plot (fig 11c).

No more vortex sheet like structures are visible at t = 6.5 (fig 12a-c). From fig. 4b, it is noted that this was the time of roll-up into a large structure. Most of the vortical structures are large, tubular and oriented randomly. The ribs are still persistent, especially the one in the center of the plot, it can be seen at all three vorticity levels, indicating that the 'ribs' have become more intense after getting stretched. At t = 7.8 (fig. 13a-d), large scale structures are no longer seen; most of the vorticity is concentrated in smaller more intense tubes which are randomly oriented.

VIII. Acoustic Estimates

Fig 14 shows the various stages of jet evolution in a reconstruction similar to fig 4.

† The primary vortex goes from top left to bottom right of the figure and loops around the jet core such that the axis of the helix is in the streamwise direction

From this pressure plot it can be seen that the uniformly varying jet core begins to collapse at t = 5.2, after the vortex pairing has occurred. The pairing mechanism seems to induce early transition. The core breakdown is seen to be the primary source of noise. In the next couple of frames Mach waves, which originate at core breakdown, can be seen propagating outwards.

Plotted in fig 15 is the total acoustic energy flux per unit area ($p' * u_r$) radiated through a quarter domain of the cylindrical shell at r = 3. This gives a rough estimate of when the acoustic energy is radiated. From this plot one sees a sharp rise in the energy flux near t = 2. This is when the initial disturbances in the shear layer propagate to r = 3. Also around t = 3 marks the growth and non-linear interactions of instability waves. The energy flux increases with time indicating that acoustic emissions increase as the helical waves grow in amplitude and interact with each other. At t = 7.2 a peak is clearly noticed, this corresponds to the fluid physics in the core around t = 4.2 - 5. So as expected the vortex pairing and the rapid breakdown of the large scale structures at core collapse cause a rise in acoustic radiations. This is similar to results seen by Mitchell et al [18], and is consistent with the premise that rapidly varying vortical structures cause most of the noise. The ensuing small scale turbulence should give higher frequency noise. At core breakdown Mach wave radiations cause most of the acoustic radiation, and this will be captured by the pressure energy flux plot around t = 8.2.

The fluctuation of p over time at a point on the $r = 3$ shell is plotted in fig 16. It can be seen that the frequency of the oscillations increases over time as the flow becomes more turbulent.

IX. Conclusions

The instability waves are tracked in time as they evolve. Large scale vortex pairing is observed which appears to hasten transition to turbulence. Mach waves are observed around the time of core collapse. The energy spectra indicate that the energy which was initially in one mode has cascaded to higher wave numbers or smaller structures. 'Rib' structures similar to those seen in incompressible mixing layer flow of Rogers and Moser

[1] are observed. This is interesting since the flow initial and boundary conditions and the governing flow equations of these flows is quite different from the mixing layer flow.

The acoustic emissions for the jet flow are estimated. It is seen that the core collapse of the jet causes increased acoustic emissions. The time series plot of the pressure perturbation at $r = 3$ shows most of the fluctuations to be low frequency waves. Slightly higher frequency is seen as turbulence develops; smaller vortices give higher frequency emissions.

X. Acknowledgements

This work is supported by a NASA Ames grant NASA/NCC2 - 5221. We also acknowledge the support of the Minnesota Supercomputer Institute.

XI. References

[1] Rogers, M. M., and Moser, R. D., " The three dimensional evolution of a plane three dimensional evolution of a plane : The Kelvin-Helmholtz roll-up", *J. Fluid Mech.*, **243**, 1992, pp. 183–226.

[2] Fourguette, D. C., Mungal, M. G., and Dibble, R. W, " Time evolution of the shear layer of a supersonic axisymmetric jet ", *AIAA Journal*, **29**(7), 1991, pp. 1123–1130.

[3] Freund, J. B., Lele, S. K., and Moin, P., " Direct simulation of a supersonic round turbulent shear layer ", Presented as Paper 97-0760 at AIAA 35th Aerospace Sciences Meeting and Exhibit, Reno, NV., 1997.

[4] Mankbadi, R. R., Hayder, M. E., and Pivonelli, L. A., " Structure of supersonic jet flow and its radiated sound ", *AIAA Journal*, **32** 1993, pp. 897–906.

[5] Moser, R. D., Moin, P., and Leonard, A., " A spectral numerical method for the Navier-Stokes equations with applications to Taylor–Couette flow ", *J. Comp. Phys.*, **52**(3), 1983, pp. 524–544.

[6] Moser, R. D., and Rogers, M. M., " The three dimensional evolution of a plane mixing layer : pairing and transition to turbulence", *J. Fluid Mech.*, **247** , 1993, pp. 275–320.

[7] Loulou, P., " Direct numerical simulation of incompressible pipe flow using a b-spline spectral method ", *Ph.D Dissertation*, Stanford University, June 1996.

[8] Sandham, N. D., & Reynolds, W. C., " Compressible mixing layer: linear theory and direct simulation ", *AIAA Journal*, **28**, 1990, pp. 618–624.

[9] Sandham, N. D., & Reynolds, W. C., " Three-dimensional simulations of large eddies in the compressible mixing layer ", *J. Fluid Mech.*, **224**, 1991, pp. 133–158.

[10] Spalart, P. R., Moser, R. D., and Rogers, M. M., " Spectral methods for the Navier-Stokes equations with one infinite and two periodic directions ", *J. Comp. Phys.*, **96**(2), 1991, pp. 297–324.

[11] Rao, R. M, " Direct numerical simulation of turbulent supersonic jets ", *Ph.D Dissertation*, University of Minnesota, Dec. 1997.

[12] De Boor, C., " *A Practical Guide to Splines* ", Springer-Verlag, 1978.

[13] Wray, A. A., " Very low storage time-advancement schemes ", Internal Report, NASA-Ames Research Center, Moffet Field, California, 1986.

[14] Shariff, K., " Comment on Coordinate Singularities by P. R. Spalart ", Personal Communication.

[15] Engquist, B., and Majda, A., " Absorbing boundary conditions for the numerical simulation of waves ", *Math. Comput.*, **31**(139), 1977, pp. 629–651.

[16] Engquist, B., and Majda, A., " Radiation boundary conditions for acoustic and elastic wave calculations ", *Commun. Pure Appl. Math.*, **32**, 1979, pp. 313–357.

[17] Giles, M. B., " Non-reflecting boundary conditions for Euler equation calculations", *AIAA Journal*, **28**, December 1990, pp. 2050–2058.

[18] Mitchell, B. E., Lele, S. K., and Moin, P., " Direct computation of the sound generated by subsonic and supersonic axisymmetric jets ", Technical Report TF-66, Department of Mechanical Engineering, Stanford University, CA, 1995.

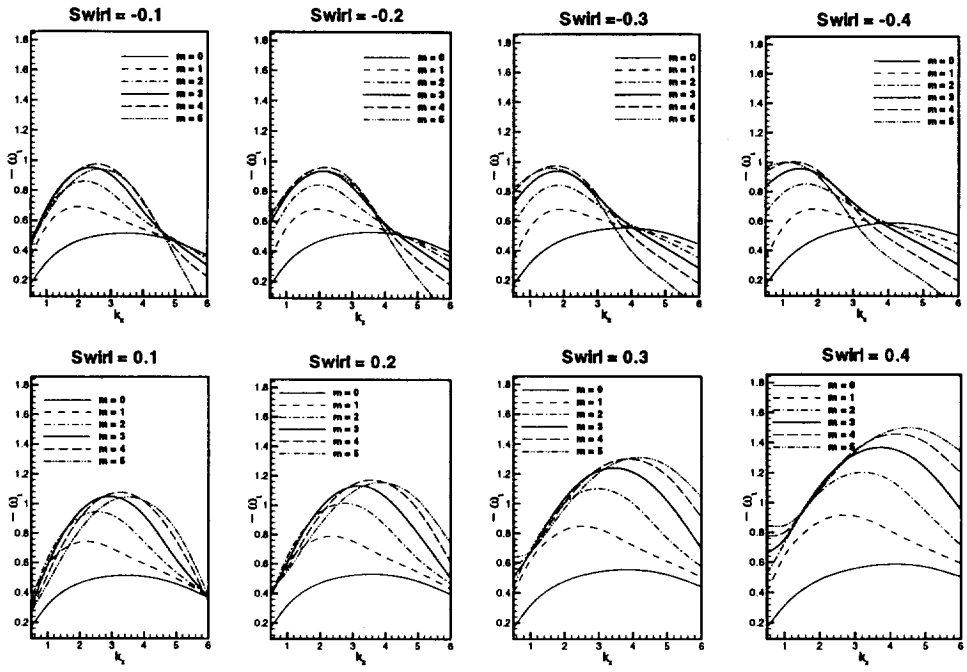

Fig. 1

Ram M Rao (Physics of Fluids)

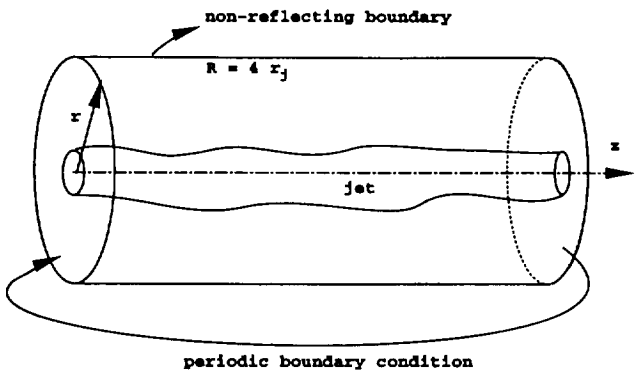

Fig. 2

Ram M Rao (Physics of Fluids)

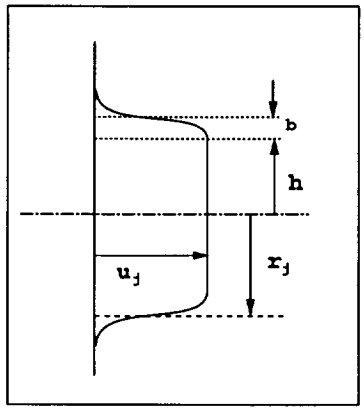

Fig. 3

Ram M Rao (Physics of Fluids)

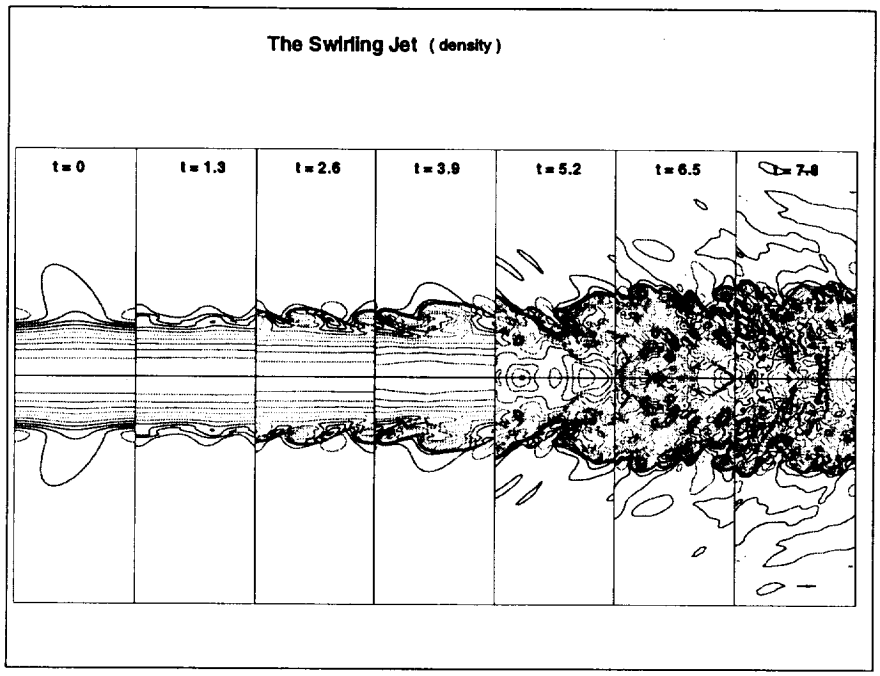

Fig. 4a

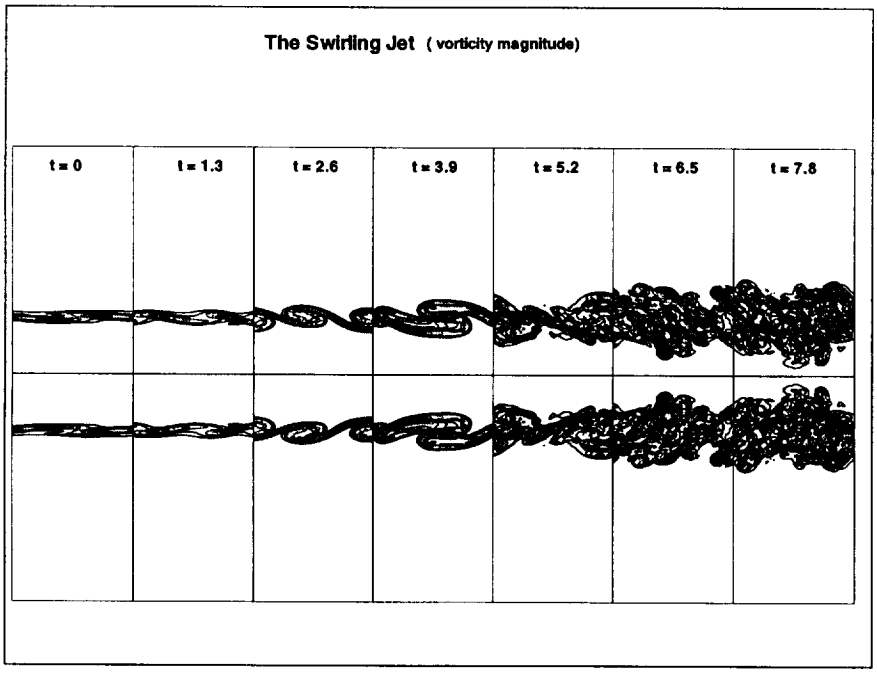

Fig. 4b

Ram M Rao (Physics of Fluids)

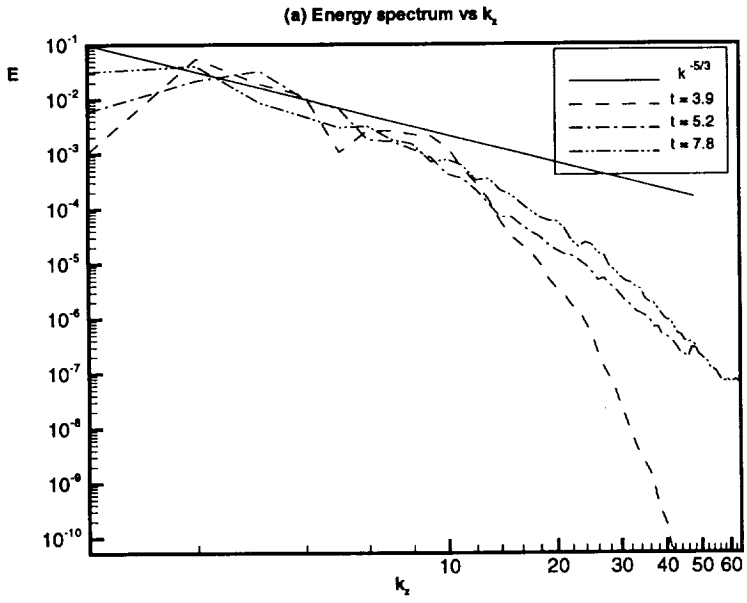

Fig. 5a

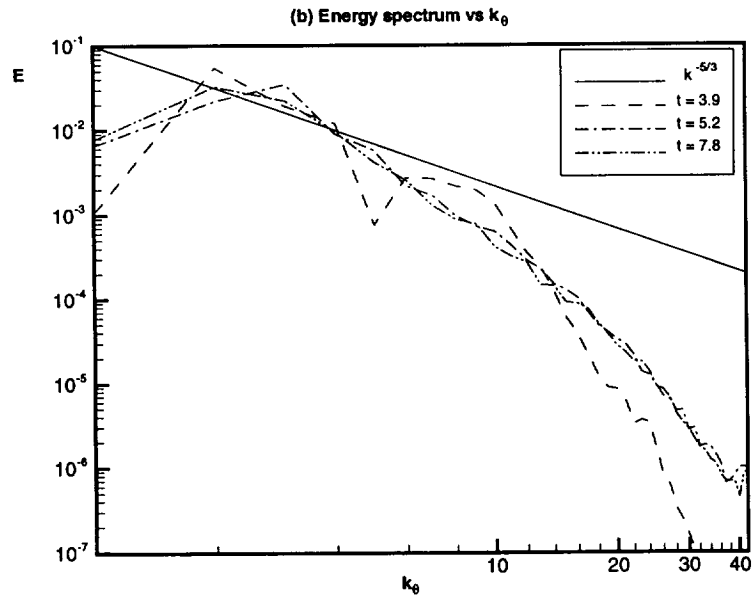

Fig. 5b

Ram M Rao (Physics of Fluids)

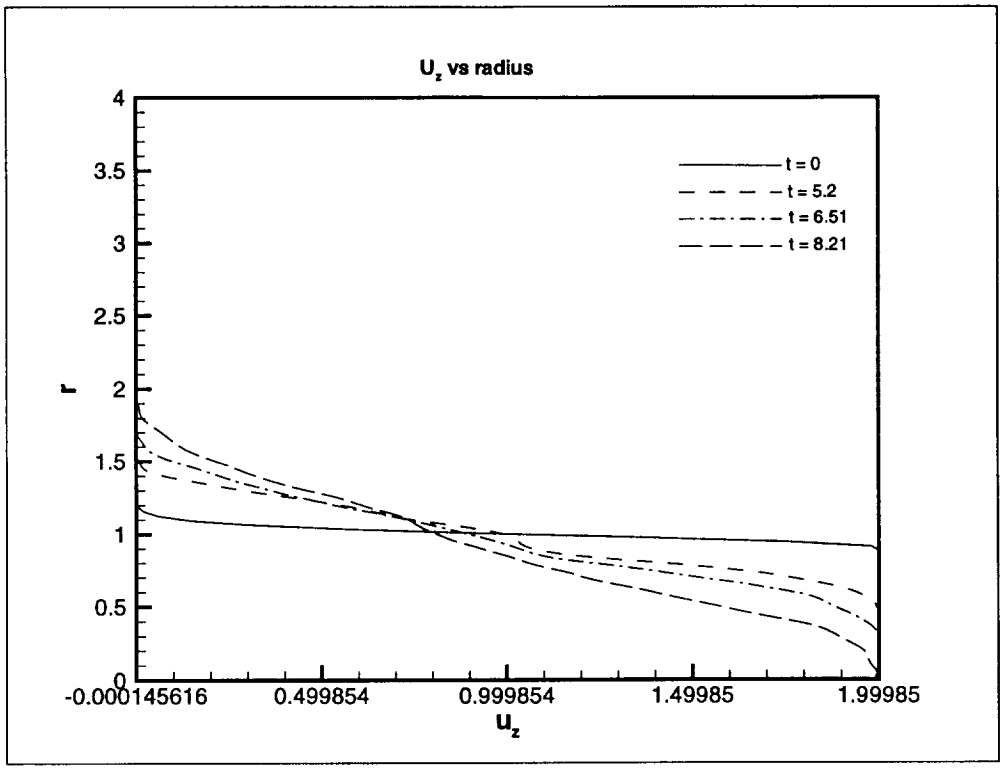

Fig. 6

Ram M Rao (Physics of Fluids)

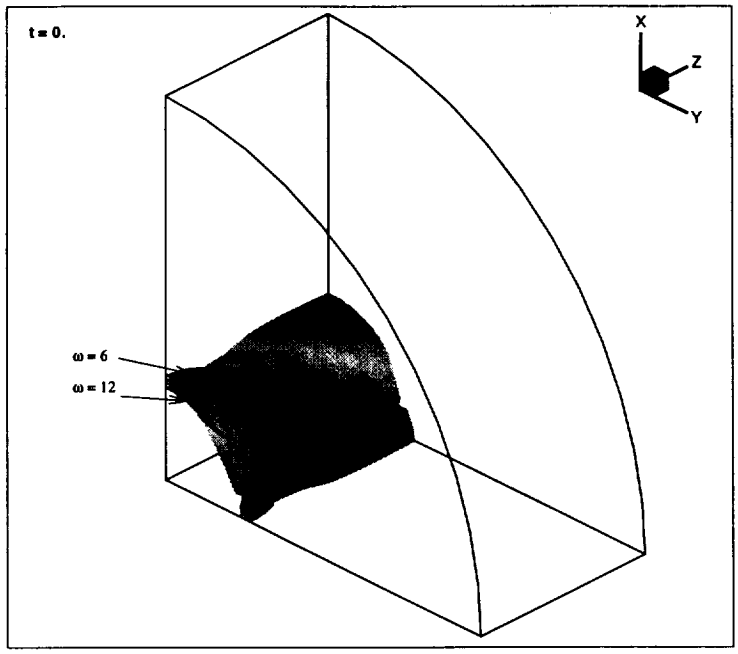

Fig. 7

Ram M Rao (Physics of Fluids)

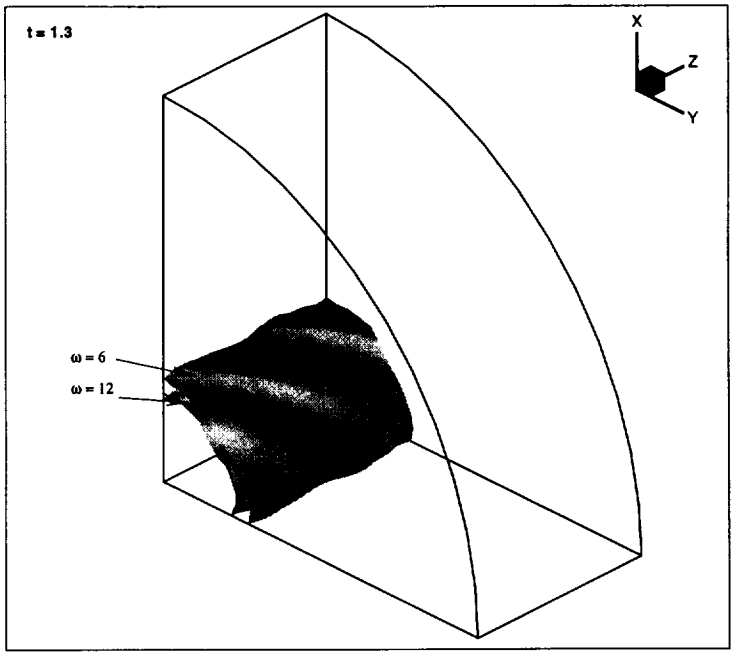

Fig. 8

Ram M Rao (Physics of Fluids)

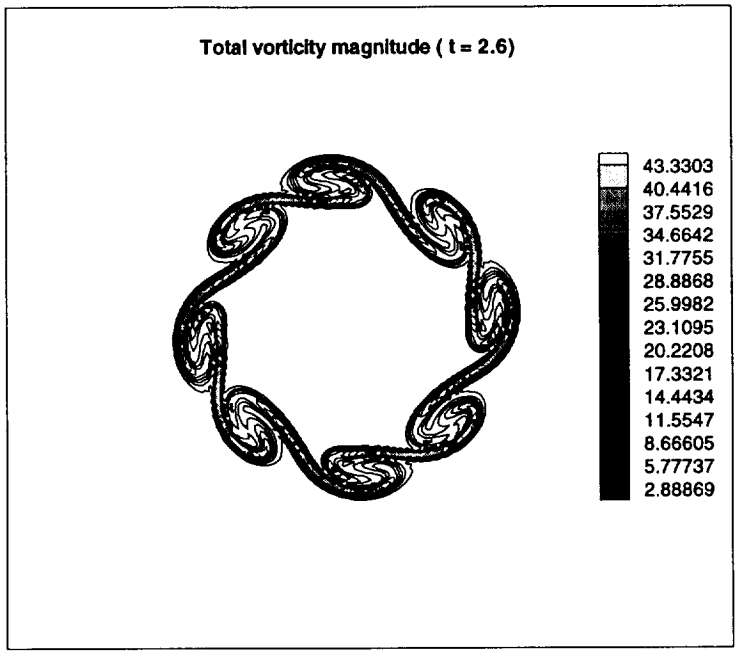

Fig. 9a

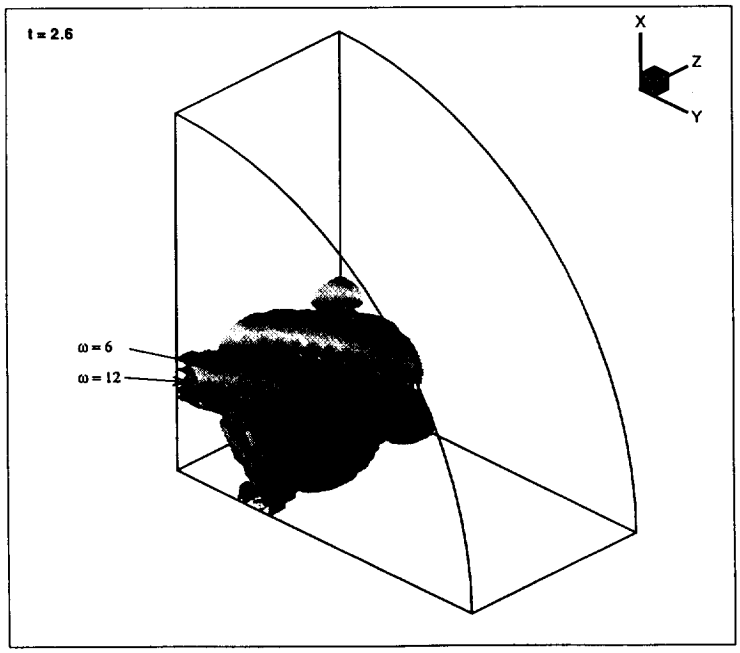

Fig. 9b

Ram M Rao (Physics of Fluids)

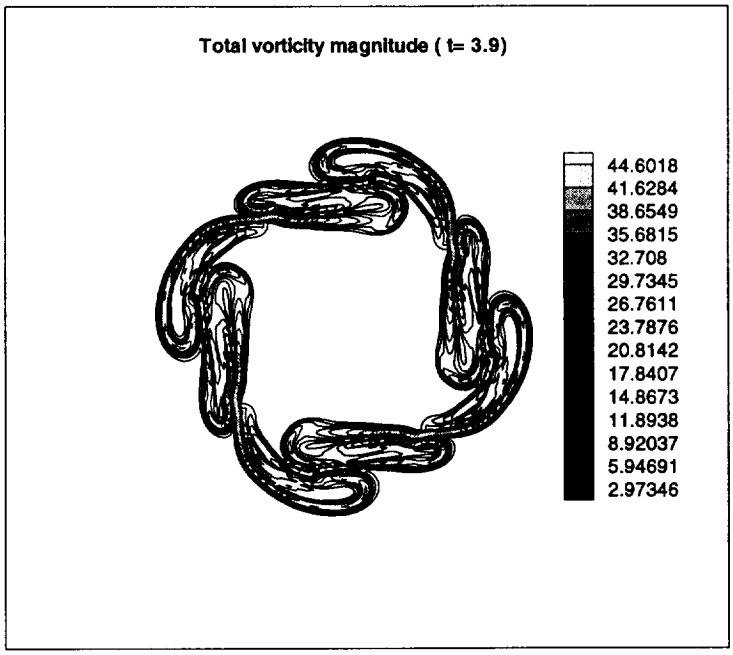

Fig. 10a

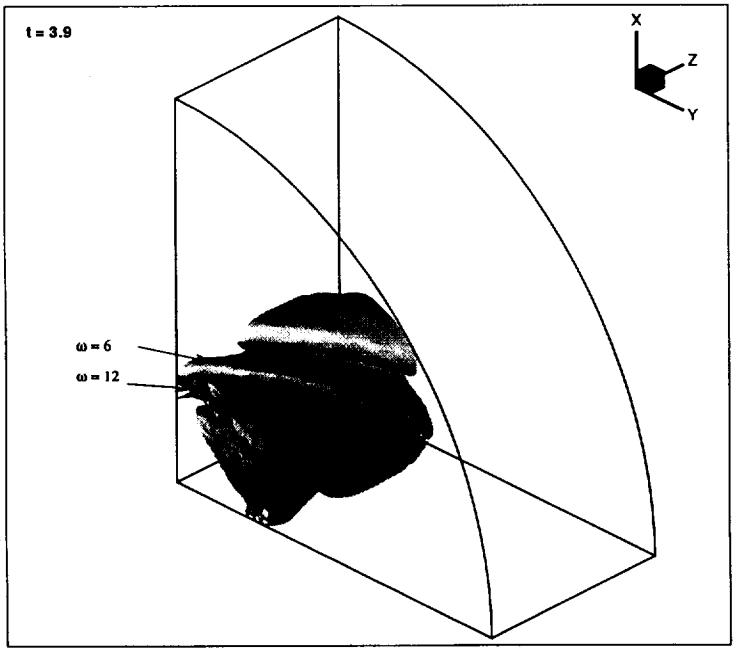

Fig. 10b

Ram M Rao (Physics of Fluids)

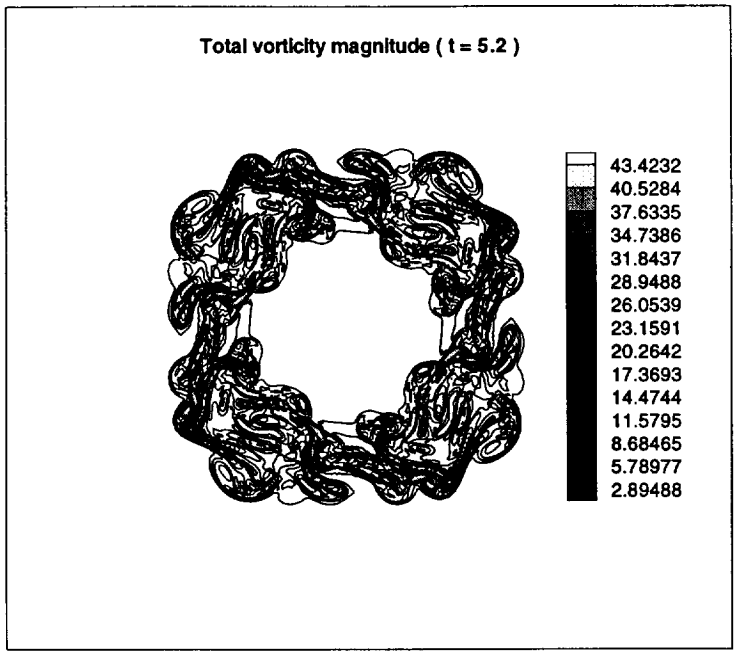

Fig. 11a

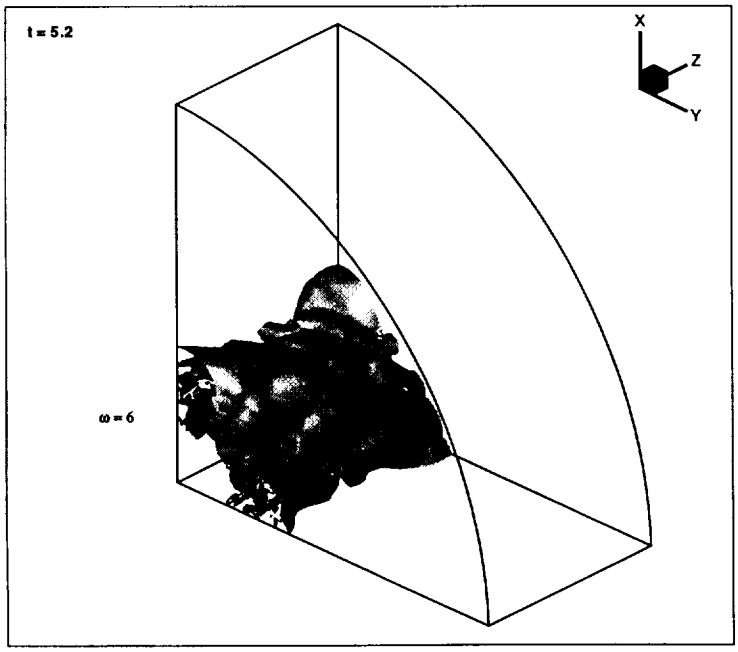

Fig. 11b

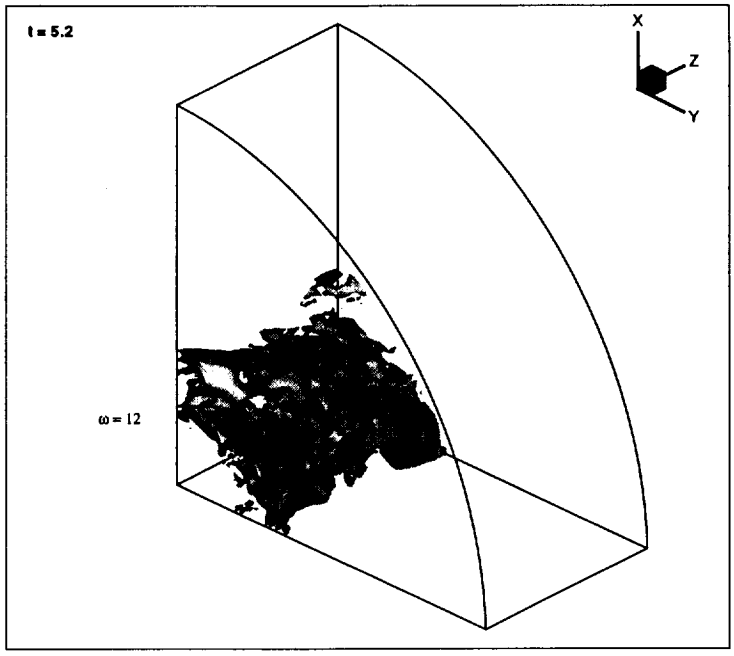

Fig. 11c

Ram M Rao (Physics of Fluids)

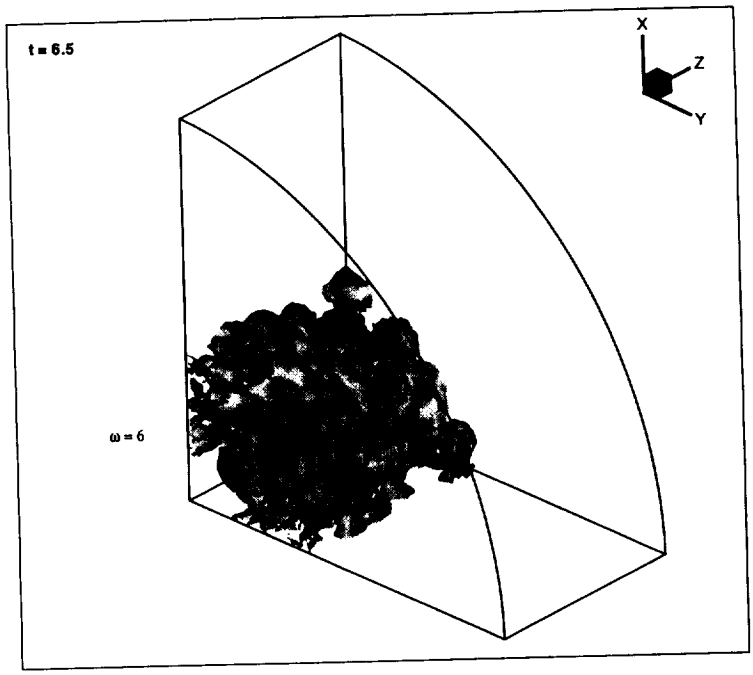

Fig. 12a

Ram M Rao (Physics of Fluids)